Dalton Transactions

Cite this: *Dalton Trans.*, 2012, **41**, 13697

www.rsc.org/dalton

PAPER

Multi-frequency EPR studies of a mononuclear holmium single-molecule magnet based on the polyoxometalate $[Ho^{III}(W_5O_{18})_2]^{9-}$

Sanhita Ghosh,[a,b] Saiti Datta,†[b] Lisa Friend,[b] Salvador Cardona-Serra,[c] Alejandro Gaita-Ariño,[c] Eugenio Coronado[c] and Stephen Hill*[a,b]

Received 25th July 2012, Accepted 21st August 2012
DOI: 10.1039/c2dt31674a

Continuous-wave, multi-frequency electron paramagnetic resonance (EPR) studies are reported for a series of single-crystal and powder samples containing different dilutions of a recently discovered mononuclear Ho^{III} ($4f^{10}$) single-molecule magnet (SMM) encapsulated in a highly symmetric polyoxometalate (POM) cage. The encapsulation offers the potential for applications in molecular spintronics devices, as it preserves the intrinsic properties of the nanomagnet outside of the crystal. A significant magnetic anisotropy arises due to a splitting of the Hund's coupled total angular momentum ($J = L + S = 8$) ground state in the POM ligand field. Thus, high-frequency (50.4 GHz) EPR studies reveal a highly anisotropic eight line spectrum corresponding to transitions within the lowest $m_J = \pm 4$ doublet, split by a strong hyperfine interaction with the $I = 7/2$ Ho nucleus (100% natural abundance). X-band EPR studies reveal the presence of an appreciable tunneling gap between the $m_J = \pm 4$ doublet states having the same nuclear spin projection, leading to a highly non-linear field-dependence of the spectrum at low-frequencies.

1. Introduction

The highly interdisciplinary research field of molecular nanomagnetism has attracted growing interest from chemists and physicists for the past two decades, dating back to the initial discovery of slow magnetization relaxation of purely molecular origin in the now famous Mn_{12}-acetate cluster.[1] Since then, extensive studies of so-called single-molecule magnets (SMMs) have resulted in a remarkable number of important fundamental discoveries, including resonant quantum tunneling of magnetization (QTM),[2,3] and Berry Phase Interference effects associated with the QTM phenomenon,[4] among many others. SMMs have also attracted much attention because of their potential technological relevance to high-density memory applications[5] and quantum information processing.[6]

Until fairly recently, most synthetic efforts were directed towards polynuclear transition metal clusters, with the goal of maximizing both the molecular spin state and magneto-anisotropy. However, a number of fundamental factors have limited progress in this area, with the record blocking temperature only just surpassing that of the original SMM, Mn_{12}.[7] The limiting factors include: (i) the tendency for the superexchange interactions between the constituent transition metal spins to be both weak and often antiferromagnetic; and (ii) the difficulties associated with controllably projecting a significant magneto-anisotropy onto the ground spin state. Indeed, careful studies of the latter issue suggested that one is unlikely to achieve anisotropy barriers that significantly exceed those of the constituent ions.[8] Thus, it was perhaps not so surprising that a major breakthrough involved the preparation, by Ishikawa *et al.*, of a SMM comprising just a single lanthanide ion sandwiched within a double-decker phthalocyanine structure.[9,10] Since this discovery, there has been an explosion in activity focused not only on lanthanides,[11–20] but also on other simple mononuclear SMMs in which the spin–orbit and ligand-field (LF) effects can be rationally optimized.[21–23]

In this work, we present a very detailed spectroscopic study of crystals of the holmium member of a family of polyoxometalate (POM) complexes, of general formula $[Ln^{III}(W_5O_{18})_2]^{9-}$,[11,12] in which the lanthanide ion is encapsulated between two W_5O_{18} POM units that provide a square-antiprismatic coordination geometry which is very similar to the original bis(phthalocyanine) lanthanide complexes reported by Ishikawa.[9] A large magnetic anisotropy is realized in these complexes due to a splitting of the spin–orbit coupled $J(= L + S)$ ground state in the POM ligand field, resulting in the observation of SMM behavior in the Ho^{III} and Er^{III} members of the family. Importantly, the encapsulation offers the potential for applications in molecular spintronics devices,[24,25] because it preserves the intrinsic SMM properties of the lanthanide ion outside of a crystal, *e.g.*, on surfaces or in field effect devices. The present study by multi-frequency electron paramagnetic resonance (EPR) represents by far the most

[a]*Department of Physics, Florida State University, Tallahassee, FL 32306, USA*
[b]*National High Magnetic Field Laboratory, 1800 E. Paul Dirac Drive, Tallahassee, FL 32310, USA. E-mail: shill@magnet.fsu.edu*
[c]*Instituto de Ciencia Molecular, Universidad de Valencia, c/Catedrático José Beltrán, 2, 46980 Paterna, Spain*
†Present address: Department of Physics, Amherst College, Amherst, MA 01002, USA.

comprehensive of its kind for this class of SMM (though plenty of examples can be found for isolated lanthanide ions – see, *e.g.*, Ref. 26), providing important insights into the hyperfine and LF interactions that dictate their low-temperature quantum dynamical properties.

2. Background

The isostructural family of compounds, $[Na^+]_9[Ln^{III}(W_5O_{18})_2]^{9-}\cdot nH_2O$ (Ln = Gd, Tb, Dy, Ho (**1**) and Er), crystallize in the centrosymmetric triclinic space group $P\bar{1}$, in which the Ln^{III} ion is encapsulated by two anionic POM $[W_5O_{18}]^{6-}$ units.[11,12] The anionic clusters are further surrounded by sodium cations (for neutrality) that are coordinated to oxygens within the cluster, as well as a large number of lattice water molecules ($n \approx 35$), thus providing good isolation between the lanthanide magnetic moments. In spite of the low crystallographic symmetry, the local coordination geometry about the Ln^{III} ion approximates to a square-antiprismatic D_{4d} LF symmetry, as can be seen with the aid of Fig. 1. The Ln^{III} is coordinated from above and below by approximately co-planar O_4^{2-} squares associated with the anionic $[W_5O_{18}]^{6-}$ units, which are twisted with respect to each other by an angle, Φ, that is very close to the ideal 45° corresponding to an exact D_{4d} symmetry. It should be emphasized, however, that the D_{4d} symmetry is not exact: the Ln^{III}–O distances are not identical, and the twisting angle, Φ, deviates slightly (by <1°) from 45° for every member of the family. Nevertheless, this approximation serves as a useful starting point for discussion of the high-frequency EPR results; a complete account requires consideration of lower symmetry LF terms.

The $[Xe]4f^{10}$ electronic configuration of Ho^{III} gives rise to a Hund's rule spin–orbit coupled ground state with $L = 6$, $S = 2$, and $J = |L + S| = 8$. The D_{4d} point group possesses an S_8 axis which is perpendicular to the O_4^{2-} squares in the case of **1**. Hence, the molecule has an approximate four-fold (C_4) rotational symmetry about this S_8 axis. However, because of the time-reversal invariance (TRI) of the zero-field (spin–orbit + LF) Hamiltonian, the magneto-anisotropy tensor typically possesses a higher symmetry than the corresponding molecule.[27,28] This consideration gives rise to a Hamiltonian with $S_8 \times C_i = C_8$ symmetry (C_i because the TRI results in an invariance with respect to inversion of the magnetic moment), for which the off-diagonal terms are at least eighth-order in the angular momentum operators. Given the restriction to sixth-order for an f-shell, one can conclude that a Ln^{III} ion with an exact D_{4d} local coordination geometry should be describable *via* a perfectly cylindrically symmetric (C_∞) LF Hamiltonian. As such, the Ho^{III} spectrum would consist of a series of eight degenerate $\pm m_J$ zero-field doublets. Such an approximation has been used to fit magnetic susceptibility ($\chi_m T$ *vs.* T) data across the full series of compounds, yielding a set of axial LF parameters.[12]

For the purposes of the present study, we express the LF Hamiltonian in terms of extended Stevens Operators $\hat{O}_k^q$ (k = 2, 4, 6, and $|q| \leq k$), with associated coefficients B_k^q,[29,30] with $\hat{O}_k^q$ expressed in terms of the total angular momentum operators $\hat{J}$ and $\hat{J}_i$ ($i = x, y, z$). Using this convention, the axial ($q = 0$) coefficients determined from magnetic measurements for the Ho^{III} compound are: $B_2^0 = 0.600\ cm^{-1}$, $B_4^0 = 6.94 \times 10^{-3}\ cm^{-1}$, $B_6^0 = -4.88 \times 10^{-5}\ cm^{-1}$. The resultant spectrum associated with the $J = 8$ ground state is displayed in Fig. 2. As can be seen, a double-well potential is realized, with the $m_J = \pm 4$ LF states lying lowest in energy, separated by 16 cm^{-1} from the first excited ($m_J = \pm 5$) states. Although the ground state does not correspond to the maximal projection of J onto the quantization axis, one might nevertheless expect to observe low-temperature magnetic bistability within this description, owing to the sizeable energy barrier separating the ±4 ground states. Indeed, the Er^{III} member of the family does exhibit tell-tale frequency-dependent peaks in its out-of-phase AC susceptibility, indicative of SMM behavior. However, the situation is not as clear-cut for Ho^{III}, pointing to possible quantum relaxation within the ground state, thus providing one of the first hints as to the limitations of the exact D_{4d} description.[12]

For the purposes of the (low-energy) EPR studies, one must also take into account the hyperfine coupling between the electron and nuclear moments. Holmium occurs naturally in only one stable form (^{165}Ho) with a nuclear spin of $I = 7/2$, providing an advantage relative to Gd, Dy and Er, which occur naturally as mixtures of isotopes with different nuclear moments. As will be seen, the hyperfine coupling for Ho^{III} is rather strong, leading to

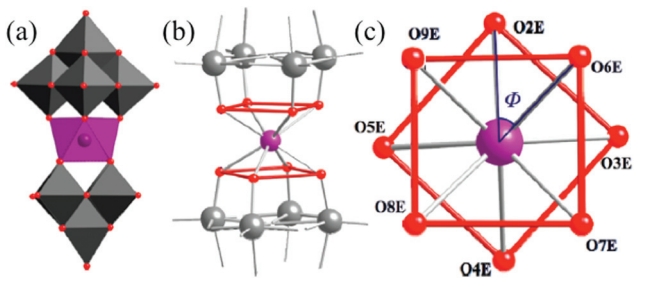

Fig. 1 (a) Polyhedral representation of the $[Ln(W_5O_{18})_2]^{9-}$ cluster. (b) Perspective showing the square-antiprismatic coordination of the central Ho^{III} ion. (c) A separate view along the axial z-direction of the coordination environment of the Ho^{III} ion; Φ (= 44.2°) represents the relative twisting angle about the z-axis of the two O_4^{2-} squares above and below Ho^{III} ion. Color code: oxygen, red; tungsten, gray; holmium, purple.

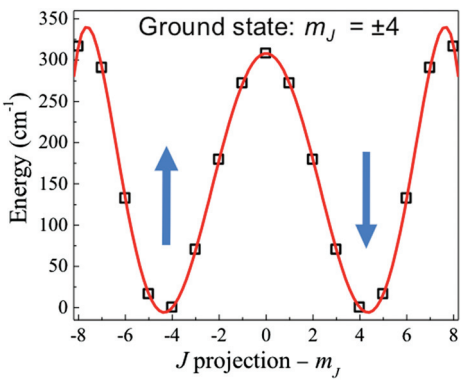

Fig. 2 Energy level diagram for **1** based on the axial LF parameterization deduced from magnetic measurements.[12] The energies are plotted as a function of the associated angular momentum projection (m_J), revealing a double-well potential. The red curve is a continuous polynomial function of the form: Energy = $B_2m^2 + B_4m^4 + B_6m^6$, where B_2, B_4 and B_6 are directly related to the axial B_k^0 Stevens coefficients.[29]

the observation of distinct electro-nuclear EPR transitions. The program EasySpin was used to simulate EPR spectra according to following spin-Hamiltonian:[30]

$$\hat{H} = \sum_{k=2,4,6} \sum_{q=0}^{k} B_k^q \hat{O}_k^q + \hat{J} \cdot \vec{A} \cdot \hat{I} + \mu_B \vec{B}_0 \cdot \vec{g} \cdot \hat{J}. \qquad (1)$$

Here, $\vec{A}$ and $\vec{g}$ respectively represent the hyperfine and Landé coupling tensors, while $\vec{B}_0$ denotes the applied static magnetic field vector.

3. Experimental details

Single-crystal, continuous-wave (cw) EPR measurements were performed on two different instruments: a home-built multi-high-frequency superheterodyne spectrometer with *in situ* two-axis sample rotation capabilities (described in ref. 31); and a commercial Bruker E580 X-band system equipped with both dielectric and dual-mode resonators. Measurements were restricted to X-band (9.4 to 9.8 GHz) and the relatively high-frequency 50.4 GHz fundamental TE011 mode of the cylindrical resonator associated with the home-built instrument; data were collected in both cases in the temperature interval from 2 to 10 K. The crystals used for this investigation were available in diluted form, $Na_9[Ho_xY_{1-x}(W_5O_{18})_2]$ (with x = 1.00 0.25, 0.10, 0.0065 and 0.001), whereby the magnetic Ho^{III} centers are interspersed within an isostructural diamagnetic Y^{III} POM host crystal. The obtained EPR spectra indicate that the dilution has little effect on crystal quality. Samples were stored prior to study in their mother liquor, then cooled relatively quickly to avoid solvent loss. Rod shaped crystals with approximate dimensions of 0.5 × 0.5 × 3 mm^3 were selected for study. Due to the low space group symmetry, extensive angle-dependent studies were required in order to precisely locate the axial symmetry direction (quantization axis). Two-axis studies were conducted in a horizontal-field, split-pair magnet. Crystals were loaded with their long dimension oriented horizontally, then rotated *via* an external stepper motor in a horizontal plane coincident with the applied field vector. The crystal orientation, ψ, was varied in 10° increments, with ψ = 0 corresponding to the applied field parallel to the long-axis of the crystal. The procedure was then repeated for different planes of rotation, χ, *via in situ* (manual) rotation of the crystal about its long axis.

4. Results and discussion

4(a) High-frequency EPR results

All of the high-frequency (50.4 GHz) measurements were performed on crystals with x = 0.25 Ho^{III} concentration. Fig. 3 displays a series of representative spectra recorded as a function of temperature. Spectra were first collected at the lowest temperature (2 K) as a function of field orientation in order to insure reasonable alignment with the axial (z-) direction for the measurements displayed in Fig. 3. As can be seen, eight evenly spaced resonances (dips in transmission) are clearly observed, corresponding to the $(2I + 1)$, $\Delta m_I = 0$ hyperfine transitions within the lowest $m_J = \pm 4$ ground state doublet. As will be seen below, further detailed angle-dependent studies provide robust support for this

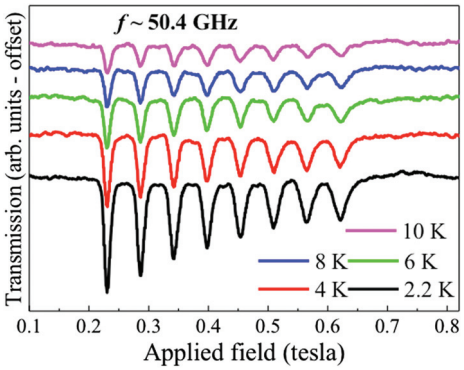

Fig. 3 Temperature dependent high-frequency EPR spectrum revealing the eight evenly spaced hyperfine transitions for an x = 0.25 sample. The field was determined (*vide infra*) to be oriented at an angle θ = 33° away from the axial (z-) direction for these measurements.

assignment, thus confirming one of the principal findings of the magnetic studies.[12] More importantly, however, the fact that these nominally forbidden $\Delta m_J = 8$ transitions are observed highlights the limitations of the purely axial (D_{4d}) description, *i.e.*, the LF Hamiltonian must contain off-diagonal ($q > 0$) terms that mix m_J levels to the extent that an EPR matrix element is generated within the ground state doublet. In fact, the observed EPR intensities are weak for a crystal of this size, at the fundamental 50.4 GHz mode of the spectrometer, suggesting that the EPR matrix element is small at this frequency. Moreover, attempts to observe a spectrum at frequencies above ~80 GHz were unsuccessful, suggesting that the $m_J = \pm 4$ states become purer (hence the EPR transitions more forbidden) upon increasing the applied field. This observation suggests a degenerate perturbation that directly connects the $m_J = \pm 4$ states, thereby allowing parallel-mode ($\Delta m_J = 0$) EPR transitions between these two states, which are strongly mixed at $B_0 = 0$, but less so as the Zeeman splitting increases. The most likely candidates would be the four-fold terms, $\hat{O}_4^4$ and $\hat{O}_6^4$. We come back to this discussion in more detail in the following section.

The $P\bar{1}$ space-group means that there are two molecules in the unit cell. However, they are related by an inversion. Consequently, their magneto-anisotropy tensors must be parallel (again due to the TRI of the spin–orbit and LF interactions), *i.e.*, from the point of view of EPR, there exists only one molecular orientation. However, it is not a trivial task to locate the molecular symmetry axis, which bears no simple relation to either the crystallographic axes or the well-defined edges of the square rod-shaped single-crystals. Thus, a series of careful two-axis rotation studies were undertaken at 2 K using a fresh crystal in order to locate the molecular symmetry axis *in situ*. This involved collecting spectra at 10° intervals for nine different planes of rotation separated by 15° (on the order of 120 independent measurements); Fig. 4 summarizes the results of these studies. The procedure required finding the field orientation with maximal projection along the quantization (z-) axis, thus producing a maximum Zeeman splitting of the $m_J = \pm 4$ doublet and, hence, a minimum in the position of the spectrum. In order to simplify the analysis, the field locations of the eight hyperfine transitions were averaged (essentially eliminating the influence of the hyperfine interaction from the spectrum) and plotted as a

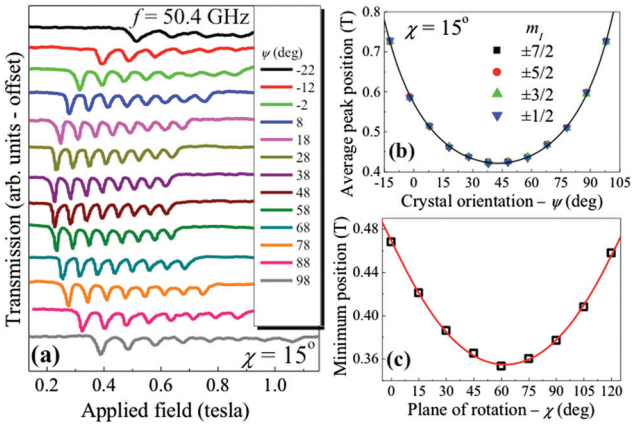

Fig. 4 Summary of the two-axis rotation studies: (a) displays a representative set of spectra recorded at 2 K as a function of the crystal orientation ψ, for one particular plane of rotation (χ = 15°); the eight peak positions from each spectrum in (a) were then averaged in $\pm m_I$ pairs, resulting in a single data point in (b) for each value of ψ; the data in (b) were then fit to the standard anisotropic g formula, $B_{res} = hf/\mu_B\sqrt{g_1^2\cos^2(\psi-\psi_o)+g_2^2\sin^2(\psi-\psi_o)}$ (B_{res} is the average peak position, f the measurement frequency, g_1 and g_2 respectively represent the maximum and minimum effective g values for each plane of rotation, and ψ_o is the crystal orientation at which the minimum in B_{res} occurs), in order to accurately determine the minimum peak position; finally, the minimum positions deduced from data sets such as those in (b) are plotted in (c) for nine different planes of rotation χ. The solid red curve in (c) is a symmetric polynomial fit on account of the fact that data points trace out a rather complex (ψ, χ) path over a sphere. The angle-dependent data set corresponding to the χ = 60° plane of rotation [closest to the minimum in (c)] was finally fit to eqn (1) in order to deduce $A_{||}$ and $g_{||}$ (Fig. 5).

function of crystal orientation, ψ, for different rotation planes, χ, as seen in Fig. 4(b) and (c). The spectrum obtained for the field orientation closest to the axial direction (χ = 60°, ψ = 52° – see Fig. 5) was then simulated with eqn (1), using the axial LF parameters determined from magnetic studies so that the only adjustable parameters were $A_{||}$ and $g_{||}$, *i.e.*, the parallel (z-) components of the hyperfine and Landé tensors which respectively determine the spacing of the eight resonances and their average positions. The best simulation was obtained with $A_{||}$ = 830 ± 10 MHz and $g_{||}$ = 1.25 ± 0.01. The obtained value for $g_{||}$ corresponds exactly to the free-ion value given by the formula (with L = 6, S = 2 and J = 8):

$$g_J = \frac{3}{2} + \frac{S(S+1) - L(L+1)}{2J(J+1)} \qquad (2)$$

As discussed further below, the simulations are more-or-less insensitive to the LF parameters so long as they yield an isolated (relative to the hyperfine and Zeeman energy scales) m_J = ±4 ground state doublet. Nevertheless, it is essential to include a $B_4^4\hat{O}_4^4$ term in order to produce a simulated spectrum, *i.e.*, there is no EPR matrix element in the absence of such an interaction. We comment further on this point in the following section.

One can achieve excellent agreement with the angle-dependence of the spectra with knowledge of only $g_{||}$, $A_{||}$ and the axial LF parameters, as seen in Fig. 5. The perpendicular interactions, $g_\perp$, $A_\perp$ and $B_4^4\hat{O}_4^4$, do not appreciably affect the positions of the

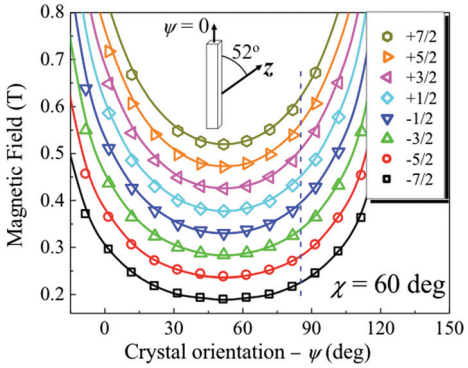

Fig. 5 Positions of the eight hyperfine peaks plotted as a function of the crystal orientation, ψ, for the χ = 60° plane of rotation (see also Fig. 4) which passes closest to the axial z-direction of the Ho^{III} POM SMMs; the data were obtained at a frequency of 50.4 GHz and a temperature of 2 K. The solid curves were generated using eqn (1) with the best-fit axial parameters (B_2^0, B_4^0, B_6^0, $A_{||}$ and $g_{||}$) given in Table 1. The inset depicts a typical rod-shaped single-crystal, with the corresponding magnetic z-direction associated with the Ho^{III} POM SMMs inclined relative to the long dimension of the sample. The dashed vertical line represents the orientation at which the spectra in Fig. 3 were collected; note that this does not coincide with a data collection angle in the present figure because the rotation planes, χ, are not the same for the two measurements.

peaks over the range where spectra could be observed, *i.e.*, up to ~60° from the axial direction. Nevertheless, a B_4^4 parameter of 94.3 MHz was included in the simulations in order to insure consistency with the X-band studies (*vide infra*). The insensitivity of the high-frequency spectra to the perpendicular interactions reflects the fact that the axial LF interactions represent the dominant source of anisotropy. Moreover, the exact values of the axial LF parameters are not so important; all that matters is that the m_J = ±4 states lie lowest in energy, isolated from higher-lying LF states. We cannot rule out anisotropies in either $\overleftrightarrow{A}$ or $\overleftrightarrow{g}$: the available data simply do not provide sufficient constraints due to the absence of spectra beyond θ = 60°, where θ is the angle between B_0 and z. Thus, $A_{||}$ and $g_{||}$ are well constrained, whereas $A_\perp$ and $g_\perp$ are not easy to determine. Careful inspection of Fig. 4(a) reveals the emergence of additional weak peaks in between the stronger resonances as the field rotates away from the axial direction (see, *e.g.*, the ψ = 88° and 98° data). This may be attributed to the effect of the transverse component of the Zeeman interaction, which mixes states in ways that give rise to additional EPR transitions. Consequently, this effect is rather sensitive to the transverse component of the Landé tensor, $g_\perp$. While it is hard to constrain $g_\perp$ on the basis of this observation, simulations suggest that it is considerably smaller than $g_{||}$. The angle-dependent measurements further reveal that the molecular quantization (z-) axis is inclined 52 ± 10° from the long axis of the rod-shaped crystals, as shown in the inset to Fig. 5; the ±10° uncertainty reflects the precision with which the sample can be aligned within the microwave cavity. Hence, it is perhaps no surprise that there was quite a significant field misalignment (θ = 33°) associated with the initial temperature dependent measurements in Fig. 3, for which only a single-axis alignment was performed.

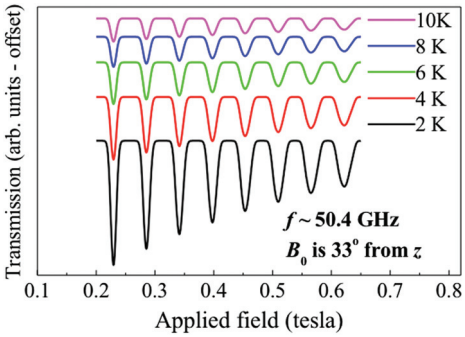

Fig. 6 Simulations of the temperature-dependent spectra presented in Fig. 3, employing eqn (1) and the parameters given in Table 1. Additional line broadening was also introduced by assuming a small distribution in the orientations of the Ho^{III} POM SMM magnetic *z*-axes, as described in the main text. This has the effect of increasing the linewidths of the higher field resonances, thus giving rise to the variation in intensity from low to high field.

Finally, we come back to the temperature dependent spectra in Fig. 3, which exhibit a fairly strong variation in peak intensity from low to high field, even at the highest temperature of 10 K. This variation cannot be explained purely on the basis of the Boltzmann populations of the hyperfine sub-levels, although this does account for a weak variation at the lowest temperatures. Examination of the peak widths suggests that sample disorder is important; the full-width-at half-maximum (FWHM) increases from low to high field, and it is this increase in peak width that is the main contributor to the decrease in intensity. In order to simulate this behavior, we considered a small Gaussian distribution (FWHM of 1°) in the orientations of the molecular *z*-axes associated with the Ho^{III} centers, which could be caused either by the alloying with Y^{III} or some other form of disorder. We note that similar forms of disorder are well documented in other SMM crystals.[32,33] The simulations, which are displayed in Fig. 6, employed the same parameters as those deduced from the angle-dependent measurements, with the addition of the disorder and a field misalignment angle $\theta = 33°$.

4(b) X-band EPR results

In the previous section, we have seen that the axial parameterization gives a good account of the high-frequency EPR spectra, with the caveat that an off-diagonal term must be included in eqn (1) to generate an EPR matrix element between the nominal $m_J = \pm 4$ ground states. For the purely axial (Ising) case, one can approximate the electronic spectrum as an effective two-level (spin-1/2) system; the LF interaction is then parameterized *via* a highly anisotropic effective *g*-tensor. However, this approach cannot capture the effects of axial symmetry breaking, which turn out to be important at low-energies/frequencies. This is seen most clearly when one attempts to predict the locations of X-band EPR transitions on the basis of an effective spin-1/2 parameterization of the high-frequency data, as seen in Fig. 7(a). Such an approach completely fails to account for the low-frequency spectrum. Consequently, one has no choice other than to solve the full 136 × 136 $[(2J + 1)(2I + 1) \times (2J + 1)(2I + 1)]$ Hamiltonian matrix corresponding to eqn (1). Moreover, in

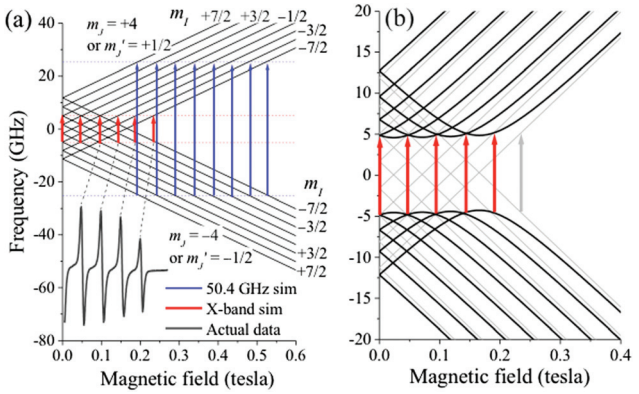

Fig. 7 Zeeman diagrams corresponding to the hyperfine-split $m_J = \pm 4$ ground states, generated at $\theta = 0$ ($B_0 \| z$) using eqn (1) with: (a) the axial parameters from Table 1 (B_2^0, B_4^0, B_6^0, $A_\|$ and $g_\|$); and (b) the full 'axial + $B_4^4\hat{O}_4^4$' parameterization (see main text for further details). Some of the levels have been labeled in (a), and the axial diagram is displayed in light gray in (b) behind the 'axial + $B_4^4\hat{O}_4^4$' diagram (black curves). The blue arrows in (a) correspond to the eight high-frequency (50.4 GHz) resonance positions observed at $\theta = 0$, deduced from the $\psi = 52°$ data points in Fig. 5. The red arrows in (a) denote the predicted X-band resonance positions based on the purely axial parameterization; agreement is poor, as can be seen from comparison with an actual single-crystal X-band spectrum at lower left [$x = 0.10$, $\theta \sim 20°$, from Fig. 8(a)]. The appearance of the large (~9 GHz) tunneling gap, or avoided level crossing, right in the middle of the 'axial + $B_4^4\hat{O}_4^4$' energy diagram in (b) results in a significant shift in the predicted X-band resonance positions (red arrows) such that they agree reasonably well with the spectrum in (a) (lower left); the gray arrow is to be compared with the highest field red arrow in (a), indicating the significant difference between the two parameterizations.

contrast to the high-frequency measurements, the X-band spectra turn out to be very sensitive to the off-diagonal ($q > 0$) LF terms (and, to a lesser extent, the diagonal ones as well). Therefore, obtaining the optimum simulation requires adjustment of many parameters. Nevertheless, such an exercise provides crucial insights into the physics of this class of molecular nanomagnet.

Because two-axis rotation was not possible with the Bruker spectrometer, single-axis rotation studies were performed on several crystals in order to obtain data with the field applied as close as possible to the *z*-axis. Angle-dependent studies and simulations (*vide infra*) again show that the EPR transitions move to lower fields upon rotating the field towards *z*. Therefore, the strategy of selecting the lowest field spectrum was again employed. Fig. 7(a) compares such a 9.64 GHz spectrum (black curve, lower left) for an $x = 0.010$ sample with the predicted peak positions (red arrows) based on the axial LF parameterization deduced from the high-frequency measurements (blue arrows); note that the commercial spectrometer outputs the derivative of the absorption spectrum due to the use of field modulation. As can be seen, such a comparison gives poor agreement: not only are the peak positions way off, but the number of peaks also differs. This cannot be attributed to a simple misalignment of the sample, *i.e.*, an improved alignment would shift the spectrum to even lower fields.

Based upon the comparison in Fig. 7(a), one might conclude that the axial LF parameterization is incorrect. However, as

noted already, off-diagonal terms must be included in eqn (1) in order to account for the finite EPR transition matrix elements. These terms necessarily connect the $m_J = \pm 4$ states, thereby altering the spectrum in the low-field region ($B_0 < 0.2$ T) in Fig. 7(a), without necessarily affecting the spectrum at higher fields. The obvious term to add to eqn (1) is $B_4^4\hat{O}_4^4$, given (i) the known deviation of the actual LF symmetry from exact D_{4d} (*i.e.*, $\Phi = 44.2°$ in **1**, see Fig. 1), and (ii) the fact that it very efficiently mixes $m_J = \pm 4$ states at 2nd order of perturbation. Remarkably, as seen in Fig. 7(b) and Fig. 8, we find that the inclusion of this one term can account nearly perfectly for the X-band spectra (parallel, perpendicular and powder), without influencing the quality of agreement with the high-frequency data. The $B_4^4\hat{O}_4^4$ perturbation lifts degeneracies between $m_J = \pm 4$ levels having the same nuclear projection, m_I, resulting in a very substantial tunneling gap of ~9 GHz right in the middle of the energy diagram, as seen in Fig. 7(b). The emergence of this gap results in a marked shift of the EPR transitions to lower fields, thereby correcting for the discrepancy between the axial simulation and experiment seen in Fig. 7(a); the axial simulation is shown in light gray in Fig. 7(b) for comparison. Importantly, the locations of the predicted 9.64 GHz transitions [red arrows in Fig. 7(b)] line up quite well with the measured spectra [Fig. 7(a)]. There remains a small discrepancy which is barely discernible in Fig. 7, though this turns out to be due to a sample misalignment of ~20°, as discussed further below.

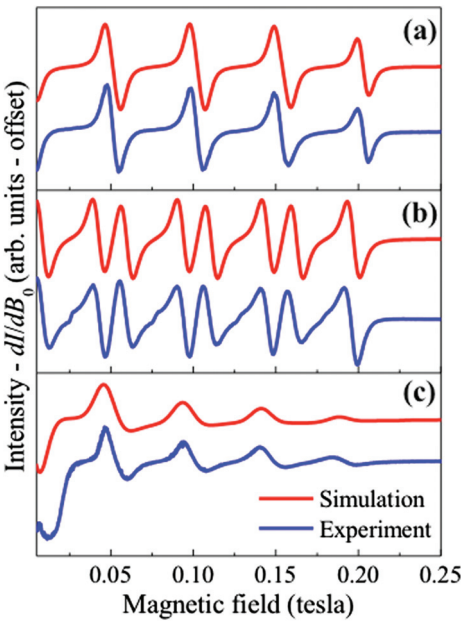

Fig. 8 Experimental and simulated X-band EPR spectra. The field range from 0–10 mT is omitted due to artifacts associated with the simulation program. The experimental spectrum in (a) was recorded using the 9.64 GHz perpendicular excitation mode ($B_1 \perp B_0$) of a dual frequency resonator at a temperature of 5 K, for a sample with $x = 0.10$ Ho^{III} concentration; the simulation also assumes perpendicular mode excitation. The experimental spectrum in (b) was recorded on the identical sample (same orientation), in the same cavity, albeit employing the parallel excitation mode at a frequency of 9.42 GHz, also at a temperature of 5 K; the simulation assumes parallel mode excitation. The experimental spectrum in (c) was obtained from a powder sample ($x = 1.00$ Ho^{III} concentration) using a perpendicular mode dielectric resonator operating at a frequency of 9.73 GHz and a temperature of 4.5 K; the simulation assumes parallel mode excitation. The parameters given in Table 1 were employed for all of the simulations, which are discussed in greater detail in the main text. Lorentzian line broadening (5 mT peak-to-peak) was included for the simulations in (a) and (b), whereas Gaussian line broadening (12 mT peak-to-peak) was used for (c), suggesting that grinding into a powder leads to a degradation of the sample purity/quality.

We next consider the nature of the observed EPR excitations. When the static field (B_0) is applied along z, the $B_4^4\hat{O}_4^4$ perturbation entangles the $m_J = \pm 4$ states (with small admixtures of $m_J = 0$ and ± 8). In such a situation, parallel mode (microwave B_1 field parallel to B_0) EPR transitions are allowed between the resulting superposition states; the $B_1 \| B_0$ magnetic dipole radiation operator connects the components of these states that have the same m_J, *i.e.*, mainly $+4 \rightarrow +4$ and $-4 \rightarrow -4$. However, the conventional perpendicular mode ($B_1 \perp B_0$) transition is completely forbidden because it connects states that differ in m_J by ± 1. This raises the obvious question as to why a spectrum is observed at all. It should be noted that the angle between B_1 and B_0 depends on the sample orientation in the high-frequency spectrometer. Thus, for nearly all orientations, both parallel and perpendicular modes are excited. However, the X-band system is equipped with cavities optimized for one or other of the excitation modes, regardless of the sample orientation. Strong spectra were recorded in both cases (Fig. 8(a) and (b)). There are several possible explanations for the observation of perpendicular mode X-band spectra. For the single-crystal measurements, the most likely scenario involves an unavoidable misalignment ($\theta \neq 0$) of the crystal. This has the effect of mixing $m_J = \pm 5$ and ± 3 character into the ground states, thereby 'switching on' the perpendicular mode matrix elements (just 10° of misalignment produces considerable EPR intensity, even when $g_\perp \ll g_\|$). In spite of considerable efforts, the best alignment achieved for single-crystal X-band measurements was $\theta = 19 \pm 1°$ (see Fig. 9). Simulations indicate plenty of perpendicular mode intensity for this field orientation (comparable to parallel mode). Thus, we were unable to examine whether the perpendicular mode transitions vanish as $\theta \rightarrow 0$.

The standard means of circumventing the crystal alignment problem is to perform measurements on a powder. Efforts to obtain a perpendicular mode powder spectrum at X-band were unsuccessful for all but the most concentrated $x = 1.00$ sample, shown in Fig. 8(c). However, the corresponding simulations employing the 'axial + $B_4^4\hat{O}_4^4$' parameterization produce absolutely no sharp features in the derivative mode spectrum over the relevant field range. In fact, there is absorption over this entire field range, but not at the turning points that contribute to peaks in the derivative; instead, the onset in intensity is rather smooth as the mis-oriented crystallites in the powder gradually begin to contribute to the absorption. Interestingly, the same parameterization produces a parallel mode powder spectrum that almost perfectly matches experiment [Fig. 8(c)]. This implies that there must be other factors beyond simple misalignment issues that contribute to the perpendicular mode intensity. For example, one cannot rule out the possibility that the LF Hamiltonian contains odd-q terms (*e.g.* $B_4^3\hat{O}_4^3$) that could also mix $m_J = \pm 5$ into the ground state, even for a perfectly aligned sample ($B_0 \| z$). One other very real possibility is that the powders and crystals used for the X-band investigations were of sufficient size that they

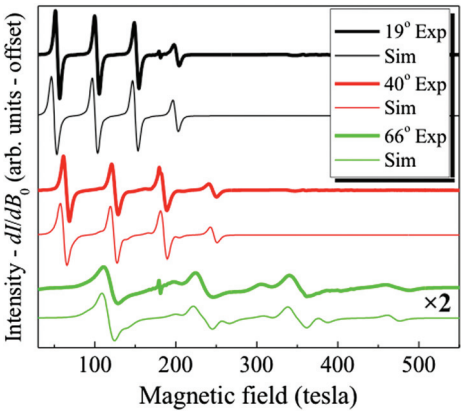

Fig. 9 Experimental (Exp) and simulated (Sim) angle-dependence of X-band spectra recorded in a dielectric perpendicular mode cavity operating at 9.75 GHz and 5 K, for a crystal with $x = 0.25\%$ Ho^{III} concentration. The field range from 0–30 mT is omitted due to artifacts associated with the simulation program. The crystal was rotated in 30° steps in a plane that was estimated to have been inclined at an angle of 18.5 ± 1° from the molecular z-axis. The first spectrum corresponds to a crystal orientation, ψ, which is ~5 ± 1° past the point of closest approach to z (*i.e.* $\theta = 18.5°$), with subsequent measurements at $\psi = 35 \pm 1°$ and $\psi = 65 \pm 1°$, corresponding to the θ values given in the legend. The parameters listed in Table 1 were employed for all of the perpendicular mode simulations, which are discussed in greater detail in the main text. Lorentzian line broadening was assumed, with a peak-to-peak width that increased from 5 to 10 mT upon rotating from 19° to 66°. This suggests an angle-dependent linewidth, similar to the case in Fig. 6, likely caused by sample disorder.

extended beyond the region in the cavity where B_1 is strictly perpendicular to B_0. Any EPR intensity arising from these two explanations ought to be rather weak, which likely explains why powder spectra were not obtained for the more dilute samples. Unfortunately, there are too many unknown factors (precise crystal orientation, LF symmetry, *etc.*) to totally resolve this issue. Overall, we obtain very satisfactory simulations for all spectra with the simple 'axial + $B_4^4\hat{O}_4^4$' parameterization. Any issues surrounding exact mode of excitation (parallel *vs.* perpendicular) seem to be explainable, though our observations do seem to leave open the possibility that additional LF terms may be important.

One of the added benefits of the dual-mode X-band resonator is that it allowed us to compare spectra at two different low frequencies for the same crystal, *i.e.*, the crystal was first aligned and spectra then recorded at the two frequencies without moving the sample. As can be seen from Fig. 8, the spectra recorded at 9.64 and 9.42 GHz are quite different. This may be attributed to the strong hyperfine coupling such that the spacing between hyperfine levels is comparable to the ~0.2 GHz shift between the two modes. Indeed, simulations account very well for both spectra, thereby providing further confidence in the parameterization. It is interesting to note that the 9.64 GHz frequency (perpendicular mode) results in the allowed $\Delta m_J = 0$ transitions occurring at points where pairs of levels are degenerate [see Fig. 8(b)]. Consequently, all but the highest field transition actually correspond to two superimposed resonances, which is the reason the intensities of these first four resonances are roughly twice that of the highest field transition. At the lower frequency of 9.42 GHz (parallel mode), the lower-field peaks are no longer degenerate [see Fig. 7(b)], resulting in a total of eight fully resolved peaks of similar intensity. These differences provided a very tight constraint on the value of B_4^4 and, thus, the magnitude of the tunneling gap observed in Fig. 7(b).

Table 1 Final parameter set used for all simulations in this work

Parameter	Value
B_0^2	18.03 GHz[a]
B_0^4	209 MHz[a]
B_0^6	−1.53 MHz[a]
B_4^4	94.3 ± 0.5 MHz
$A_\parallel$	830 ± 10 MHz
$A_\perp$	Undetermined
$g_\parallel$	1.25 ± 0.01
$g_\perp$	<0.7

[a] The uncertainty on these numbers was not determined due to the insensitivity of the spectra to their values.

Finally, angle-dependent 9.7 GHz spectra are displayed together with simulations in Fig. 9. As the field tilts away from the z-direction, additional features begin to emerge on either side of the 2nd and 3rd peaks; a similar trend was also noted in Fig. 4(a). The simulation of these features was again found to be highly dependent on the perpendicular component of the Landé tensor, $g_\perp$. Moreover, the X-band simulations exhibit some sensitivity to the axial LF parameters. Indeed, it proved impossible to account precisely for the complete set of measurements presented in Fig. 7–9 using the original LF parameters deduced from magnetic studies.[12] However, a slight adjustment in their values yielded excellent agreement with not only the data in Fig. 9, but all other measurements presented in this work. The final parameter set used for the combined simulations is given in Table 1.

Interestingly, a theoretical calculation based on a point-charge electrostatic model has allowed us to estimate the terms of the LF Hamiltonian.[34] Such a model parameterizes the crystal field effect generated by the atoms coordinated to the central lanthanide ion. The calculation confirms that $m_J = \pm 4$ is the ground state doublet, with $m_J = \pm 3$ and ± 5 as the first excited levels, and also emphasizes the importance of a fourth-order off-diagonal parameter. This simple model further predicts a ground state tunneling gap of 0.1 cm^{-1} and a separation from the $m_J = \pm 5$ and ± 3 excited states of 12 and 17 cm^{-1}, respectively. A more realistic model based on Radial Effective Charges (REC) instead of point-charges has recently been developed to provide a full description of the lowest sublevels of lanthanide single-molecule magnets.[35] Using this correction, the calculated tunneling gap increases to 0.4 cm^{-1} (12 GHz) and the excited $m_J = \pm 5$ and ± 3 states are situated at 35 and 55 cm^{-1} relative to the ground state, respectively. These findings are fully consistent with the EPR results presented in the present work. In particular, the tunneling gap, which is very well constrained from the X-band measurements, is in excellent agreement with the REC theory. Moreover, this model predicts a mixing on the order 1% of the $m_J = \pm 3$ and ± 5 states into the ground-state wavefunction, which could very well be responsible for the 'forbidden' EPR

transitions that are observed. These appear as a consequence of the off-diagonal B_2^1 and B_4^3 parameters, due to the distorted D_{4d} geometry of the complex.

5. Summary and conclusions

We have presented a comprehensive EPR study of the low-energy spectrum of a Ho^{III} member of a new class of mononuclear lanthanide SMMs. Exceptionally good agreement is achieved between simulations and an extensive array of measurements performed at multiple frequencies, for different crystal orientations (and a powder), using a single set of magnetic Hamiltonian parameters given in Table 1. Although there remains some softness in the final LF parameter set, particularly with regard to the axial terms, one can arrive at several extremely robust conclusions concerning the spectrum of this mononuclear Ho^{III} SMM: the ground LF states correspond to the nominal $m_J = \pm 4$ projections split into eight m_I sub-levels through the hyperfine coupling to the $I = 7/2$ nuclear spin; a very considerable tunneling gap of ~9 GHz is generated at zero-field *via* the off-diagonal part of the LF Hamiltonian, which efficiently connects the $m_J = \pm 4$ states; and well resolved EPR transitions are observed, corresponding to distinct coupled electron-nuclear excitations.

The above conclusions suggest several interesting prospects with regards to the low-temperature quantum dynamics of this Ho^{III} SMM. The large tunneling gap raises the possibility of observing coherent zero-field tunneling dynamics, especially given the opportunities for dramatically reducing dipolar decoherence through dilution of the Ho^{III} spins and removal of essentially all of the detrimental nuclear moments through non-magnetic isotope purification. Therefore, coherence studies of these and other members of the Ln POM family of SMMs will be performed in the future using pulsed EPR experiments to study the suitability of these molecules as spin qubits. This includes EPR studies on modified versions of these compounds, such as the $[Ln(\beta_2\text{-}SiW_{11}O_{39})_2]^{13-}$ family,[12] to determine the extent to which the LF can be 'engineered' in order to tune the quantum dynamics, especially with a view to future device applications.

Acknowledgements

We thank E. del Barco and S. Bertaina for helpful discussions. A portion of this work was carried out at the National High Magnetic Field Laboratory, which is funded by the US National Science Foundation through Cooperative Agreement DMR0654118 and by the State of Florida. SH acknowledges the support of the NSF (grant # CHE0924374). The work in Spain has been supported by the European Union (Project ELFOS and ERC Advanced Grant SPINMOL), the Spanish MINECO (Project CONSOLIDER-INGENIO on Molecular Nanoscience, and Projects MAT2007-61584, and MAT2011-22785 co-financed by FEDER) and the Generalidad Valenciana (PROMETEO Program).

References

1 A. Caneschi, D. Gatteschi, R. Sessoli, A. L. Barra, L. C. Brunel and M. Guillot, *J. Am. Chem. Soc.*, 1991, **113**, 5873.
2 J. R. Friedman, M. P. Sarachik, J. Tejada and R. Ziolo, *Phys. Rev. Lett.*, 1996, **76**, 3830.
3 L. Thomas, F. Lionti, R. Ballou, D. Gatteschi, R. Sessoli and B. Barbara, *Nature*, 1996, **383**, 145.
4 W. Wernsdorfer and R. Sessoli, *Science*, 1999, **284**, 133.
5 G. Christou, D. Gatteschi, D. N. Hendrickson and R. Sessoli, *MRS Bulletin*, 2000, 66.
6 M. N. Leuenberger and D. Loss, *Nature*, 2001, **410**, 789.
7 C. J. Milios, A. Vinslava, W. Wernsdorfer, S. Moggach, S. Parsons, S. P. Perlepes, G. Christou and E. K. Brechin, *J. Am. Chem. Soc.*, 2007, **129**, 2754.
8 S. Hill, S. Datta, J. Liu, R. Inglis, C. J. Milios, P. L. Feng, J. J. Henderson, E. del Barco, E. K. Brechin and D. N. Hendrickson, Perspectives article in themed issue, *Dalton Trans.*, 2010, **39**, 4693–4707.
9 N. Ishikawa, M. Sugita, T. Ishikawa, S.-y. Koshihara and Y. Kaizu, *J. Am. Chem. Soc.*, 2003, **125**, 8694.
10 N. Ishikawa, M. Sugita and W. Wernsdorfer, *J. Am. Chem. Soc.*, 2005, **127**, 3650.
11 M. AlDamen, J. M. Clemente-Juan, E. Coronado, C. Martí-Gastaldo and A. Gaita-Ariño, *J. Am. Chem. Soc.*, 2008, **130**, 8874.
12 M. AlDamen, S. Cardona-Serra, J. M. Clemente-Juan, E. Coronado, A. Gaita-Ariño, C. Martí-Gastaldo, F. Luis and O. Montero, *Inorg. Chem.*, 2009, **48**, 3467.
13 P. H. Lin, T. J. Burchell, L. Unger, L. F. Chibotaru, W. Wernsdorfer and M. Murugesu, *Angew. Chem., Int. Ed. Engl.*, 2009, **48**, 9489.
14 F. Luis, M. J. Martínez-Pérez, O. Montero, E. Coronado, S. Cardona-Serra, C. Martí-Gastaldo, J. M. Clemente-Juan, J. Sesé, D. Drung and T. Schurig, *Phys. Rev. B*, 2010, **82**, 060403.
15 S.-D. Jiang, B.-W. Wang, H. L. Sun, Z.-M. Wang and S. Gao, *J. Am. Chem. Soc.*, 2011, **133**, 4730.
16 J. Long, F. Habib, P. H. Lin, I. Korobkov, G. Enright, L. Ungur, W. Wernsdorfer, L. F. Chibotaru and M. Murugesu, *J. Am. Chem. Soc.*, 2011, **133**, 5319.
17 J. D. Rinehart, M. Fang, W. Evans and J. R. Long, *Nat. Chem.*, 2011, **3**, 538.
18 A. Watanabe, A. Yamashita, M. Nakano, T. Yamamura and T. Kajiwara, *Chem.–Eur. J.*, 2011, **17**, 11195.
19 M. J. Martínez-Pérez, S. Cardona-Serra, C. Schlegel, F. Moro, P. J. Alonso, H. Prima-García, J. M. Clemente-Juan, M. Evangelisti, A. Gaita-Ariño, J. Sesé, J. van Slageren, E. Coronado and F. Luis, *Phys. Rev. Lett.*, 2012, **108**, 247213.
20 J. D. Rinehart, M. Fang, W. J. Evans and J. R. Long, *J. Am. Chem. Soc.*, 2011, **133**, 14236.
21 D. E. Freedman, W. H. Harman, T. D. Harris, G. J. Long, C. J. Chang and J. R. Long, *J. Am. Chem. Soc.*, 2010, **132**, 1224.
22 D. Weismann, Y. Sun, Y. Lan, G. Wolmersh, A. K. Powell and H. Sitzmann, *Chem.–Eur. J.*, 2011, **17**, 4700.
23 J. D. Rinehart and J. R. Long, *J. Am. Chem. Soc.*, 2009, **131**, 12558.
24 J. Lehmann, A. Gaita-Ariño, E. Coronado and D. Loss, *Nat. Nanotechnol.*, 2007, **2**, 312.
25 J. M. Clemente-Juan, E. Coronado and A. Gaita-Ariño, *Chem. Soc. Rev.*, DOI: 10.1039/C2CS35205B.
26 S. Bertaina, S. Gambarelli, A. Tkachuk, I. N. Kurkin, B. Malkin, A. Stepanov and B. Barbara, *Nat. Nanotechnol.*, 2007, **2**, 39.
27 J. Liu, E. del Barco and S. Hill, *Phys. Rev. B*, 2012, **85**, 012406.
28 J. Liu, PhD thesis, University of Florida, 2012.
29 C. Rudowicz and C. Y. Chung, *J. Phys.: Condens. Matter*, 2004, **16**, 5825.
30 S. Stoll and A. Schweiger, *J. Magn. Reson.*, 2006, **178**(1), 42–55.
31 S. Takahashi and S. Hill, *Rev. Sci. Instrum.*, 2005, **76**, 023114.
32 S. Hill, R. S. Edwards, S. I. Jones, J. M. North and N. S. Dalal, *Phys. Rev. Lett.*, 2003, **90**, 217204.
33 S. Takahashi, R. S. Edwards, J. M. North, S. Hill and N. S. Dalal, *Phys. Rev. B*, 2004, **70**, 094429.
34 J. J. Baldovi, S. Cardona-Serra, J. M. Clemente-Juan, E. Coronado and A. Gaita-Ariño, *J. Am. Chem. Soc.*, submitted.
35 J. J. Baldovi, J. M. Clemente-Juan, E. Coronado and A. Gaita-Ariño, *Dalton Trans.*, DOI: 10.1039/C2DT31411H.

